Fuel 156 (2015) 54–62

Contents lists available at ScienceDirect

Fuel

journal homepage: www.elsevier.com/locate/fuel

# Photooxidative–extractive deep desulfurization of diesel using Cu–Fe/$TiO_2$ and eutectic ionic liquid

Hayyiratul Fatimah Mohd Zaid [a,*], Fai Kait Chong [a], Mohamed Ibrahim Abdul Mutalib [b]

[a] Department of Fundamental & Applied Sciences, Universiti Teknologi PETRONAS, 32610 Bandar Seri Iskandar, Perak, Malaysia
[b] Department of Chemical Engineering, Universiti Teknologi PETRONAS, 32610 Bandar Seri Iskandar, Perak, Malaysia

## HIGHLIGHTS

- Catalyst average recyclability was 99.75%.
- 100% sulfur conversion using 2.0_Cu–Fe/$TiO_2$ for model oil and diesel fuel using.
- Sulfur removal for model oil was 97.06% and 2.94% in the 1st and 2nd extraction.
- Sulfur removal for diesel fuel was 78.93% and 21.07% in the 1st and 2nd extraction.
- Extractant used was choline chloride eutectic based ionic liquid.

## ARTICLE INFO

*Article history:*
Received 7 January 2015
Received in revised form 11 April 2015
Accepted 14 April 2015
Available online 23 April 2015

*Keywords:*
Desulfurization
Iron
Copper
Titanium dioxide
Hydrogen peroxide
Eutectic based ionic liquid

## ABSTRACT

An efficient photooxidative–extractive system for deep desulfurization of model fuel and actual diesel fuel was explored. A series of bimetallic Cu–Fe/$TiO_2$ photocatalysts was synthesized using sol–gel hydrothermal method and characterized using thermogravimetric analysis (TGA), X-ray diffraction (XRD), field emission scanning electron microscopy (FESEM) coupled with energy dispersive X-ray analysis (EDX), high resolution transmission electron microscopy (HRTEM) and diffuse reflectance UV–visible spectroscopy (DR-UV–Vis). The photocatalysts were evaluated for photooxidative–extractive deep desulfurization of model oil (100, 300 and 500 ppm dibenzothiophene in dodecane) and actual diesel fuel. 2.0 wt% Cu–Fe/$TiO_2$ photocatalyst was identified as the most efficient photocatalyst for the conversion of sulfur species under mild conditions in the presence of hydrogen peroxide ($H_2O_2$:S molar ratio of 4) as oxidant and eutectic based ionic liquid as extractant. The sulfur conversion in both model oil and actual diesel fuel reached 100%. The removal of sulfur species from both model oil and actual diesel fuel was done by two times extraction with a removal of 97.06% and 78.93%, respectively in the first run and 2.94% and 21.07%, respectively in the second run. The photocatalyst was able to be recycled for six cycles with an average performance of 99.75%.



## 1. Introduction

In fuel combustion process, sulfur species in fuel are transformed into sulfur oxides ($SO_x$), causing air pollution and acid rain which can accelerate the erosion of historical buildings, destruction of forests and endangering marine lives. In order to reduce the negative effects on human health and the environment, reduction of sulfur content in fuel is desirable [1].

The conventional process for removing sulfur species is hydrodesulfurization (HDS). However, HDS requires high temperature (320–380 °C), high pressure (3–7 MPa) and the need to use expensive hydrogen gas. Moreover, HDS is less effective when it comes to removing refractory sulfur species such as benzothiophenes, and their alkylated derivatives [2]. The major sulfur species in diesel fuel are the alkyl dibenzothiophene. Due to steric hindrance of the alkyl groups, these sulfur species are considered to be the most refractory sulfur species during HDS [3]. As the regulation for sulfur content in gasoline and diesel fuel becomes more stringent, down to 10 ppm (Euro V), it is impossible to employ the conventional HDS to fulfill the requirement. Therefore, alternative methods need to be identified. Several technologies such as oxidative desulfurization (ODS) [4,5], extractive desulfurization (EDS) [6,7], biodesulfurization (BDS) [8,9] and adsorption [10,11] have been used to remove sulfur species from fuel oil. ODS is considered to be one of the new methods investigated for deep

* Corresponding author. Tel.: +60 5 3687688; fax: +60 53655905.
*E-mail address:* hayyiratulfatimah@yahoo.com (H.F. Mohd Zaid).

http://dx.doi.org/10.1016/j.fuel.2015.04.023
0016-2361/

desulfurization. Lu et al. [12] reported that deep desulfurization using [Bmim]$PF_6$ as the extractant and Anderson-type catalyst $[(C_4H_9)_4N]_4NiMo_6O_{24}H_6$ to oxidize the sulfur could remove 98% of the dibenzothiophene (DBT) from model diesel at 30 °C in 3 h with the presence of hydrogen peroxide. It was also reported that Anderson-type catalyst $[(C_{18}H_{37})_2N(CH_3)_2]_5[IMo_6O_{24}]$ could reach 100% conversion of DBT in 10 h using molecular oxygen as the oxidant under mild reaction conditions [13]. Photooxidative reaction using the free and abundant sunlight is also a promising option. Matsuzawa et al. [14], reported that DBT and 4,6-dimethyldibenzothiophene can be oxidized to sulfoxide and sulfone using titanium dioxide ($TiO_2$) as the photocatalyst. $TiO_2$ has also been employed under UV radiation as the photocatalyst for removal of sulfur species from fuel gas with efficiencies as high as 98.5% [15]. In model gasoline, photooxidation in the presence of $O_2$ followed by acetonitrile extraction gave 97.4% sulfur removal [16]. However, these processes require UV radiation making them more difficult for deployment. Therefore, there is a need to develop a photocatalyst system that enables the use of renewable energy resources such as sunlight which provides cleaner and more efficient removal of sulfur species from petroleum fuel oils. Incorporation of transition metal onto $TiO_2$ structure could produce photocatalyst that displays activity in visible light. Iron (Fe) and copper (Cu) have received much attention as metal dopants as these metals are cheap and abundant in supply. A great deal of research have been conducted using Cu or Fe doped $TiO_2$, but co-doped Cu and Fe onto $TiO_2$ is rarely reported. Zhang [17] and Liu et al. [18] have reported that Cu and Fe co-doping $TiO_2$ led to significant absorption of visible light and a better photo-activity compared to un-doped $TiO_2$.

Ionic liquids (ILs) are salts that are liquid below 100 °C. They are of interest because of their negligible vapor pressure, non flammability, unusual solvent properties and tunability for task-specific application. Many have reported on the use of ILs in deep desulfurization of model oil and diesel fuel. 1-butyl-3-methylimidazolium trifluoromethanesulfonate ([BMIM][Otf]) has been reported for deep desulfurization of model gasoline and model diesel. It was able to remove 96% and 93% of thiophene from model gasoline and model diesel, respectively. It was also reported that [BMIM][Otf] was able to remove 97.5% of DBT from model diesel [19]. Other ILs such as 1-ethyl-3-methylimidazolium thiocyanate ([EMIM][SCN]) has also been studied giving 94% and 88% removal of thiophene in model gasoline and model diesel, respectively. In addition, [EMIM][SCN] could remove DBT completely from the diesel fuel [20]. These ILs however, are quite difficult to synthesize and therefore extremely expensive. Key requirement for a new solvent is that it should be low in cost, high solute solubility, has a wide potential window, environmental compatibility and easy to synthesize. Eutectic based ionic liquid has the potential to fulfill these criteria.

Another alternative would be to employ photooxidative–extractive process. Zhao et al. [21] used a quaternary ammonium IL, $Et_3NHCl.FeCl_3$ as an extractant combined with $TiO_2$ photooxidation under UV radiation. More than 98% desulfurization was observed for gasoline. The disadvantage of utilizing metal-based ILs is the possibility of complex formation that is soluble in gasoline which could degrade its quality. ILs synthesized from glycerol can be employed effectively at ambient temperature as extractant that can be recycled. Therefore, quaternary ammonium-glycerol ILs [22,23] could be an excellent candidate to replace current ILs. In this study choline chloride-glycerol ionic liquid (CG IL) was employed as an extractant. It was synthesize according to procedure reported by Abbot et al. [22].

Analyzing and quantifying sulfur species in very low concentration is very difficult. It is very important to select proper methods for the determination of sulfur concentration in desulfurized fuel. Gas chromatograph (GC) coupled with sulfur selective detectors such as flame photometric detector (FPD), pulsed flame photometric detector (PFPD), atomic emission detector (AED) or sulfur chemiluminescene detector (SCD) have been used for the quantitative estimation of sulfur species in commercial fuel [24]. In this study GC-SCD was used to quantify sulfur removal.

This paper focused on the development of Cu–Fe/$TiO_2$ photocatalyst for the photooxidation of sulfur species in model oil and actual diesel fuel. The photooxidized sulfur species were further extracted with CG IL. Reaction parameters include, total Cu–Fe metal loading, $H_2O_2$ amount, photocatalyst loading and initial DBT concentration in model oil. Recycling studies on Cu–Fe/$TiO_2$ was also investigated. The optimized Cu–Fe/$TiO_2$ was further employed for deep desulfurization of actual diesel fuel.

## 2. Materials and methods

### 2.1. Materials and reagents

Titanium tetraisopropoxide, TTIP **($Ti(OC_3H_7)_4$)**, n-heptane **($C_7H_{16}$)**, anhydrous iron(III) chloride **($FeCl_3$)**, copper(II) chloride dihydrate **($CuCl_2{\cdot}2H_2O$)**, dibenzothiophene, DBT **($C_{12}H_8S$)** and dodecane **($C_{12}H_{26}$)**, were supplied by Merck (Germany). All chemicals were used without further purification.

### 2.2. Synthesis of $TiO_2$

Nanoparticle $TiO_2$ was synthesized using a method modified from that reported by Khan et al. [25]. 27.0 mL of titanium tetraisopoxide (TTIP) was added into 100 mL of *n*-heptane as a solvent. The mixture was stirred at 300 rpm for 2 h. Then 7.98 mL of distilled water was added drop wise to the mixture with a molar ratio of 1:5 for TTIP:$H_2O$ and was left to age for 72 h at room temperature. The obtained sol was transferred to a 100 mL Teflon-lined autoclave vessel and was heated to 240 °C for 12 h. The resulting precipitate was dried in the oven at 70 °C for 12 h. After drying, the raw $TiO_2$ was calcined in a furnace at 400, 500 and 600 °C in ambient air for 1 h. These calcination temperatures were estimated from the TGA profile in Fig. 1. The calcination process was carried out to remove any residual organic substance and also as an activation process to transform the hydroxides into anatase $TiO_2$. The optimum calcinations temperature was selected based on the XRD patterns of the sample in Fig. 2(a). The denotation of the photocatalysts was: T_$TiO_2$, where 'T' represents the calcination temperature in °C. For example, 500_$TiO_2$ represents raw $TiO_2$ calcined at 500 °C.

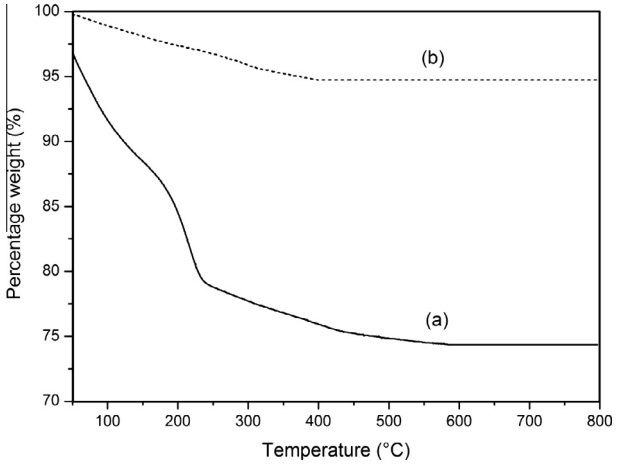


**Fig. 1.** Thermograms of (a) raw $TiO_2$ and (b) 500_$TiO_2$.

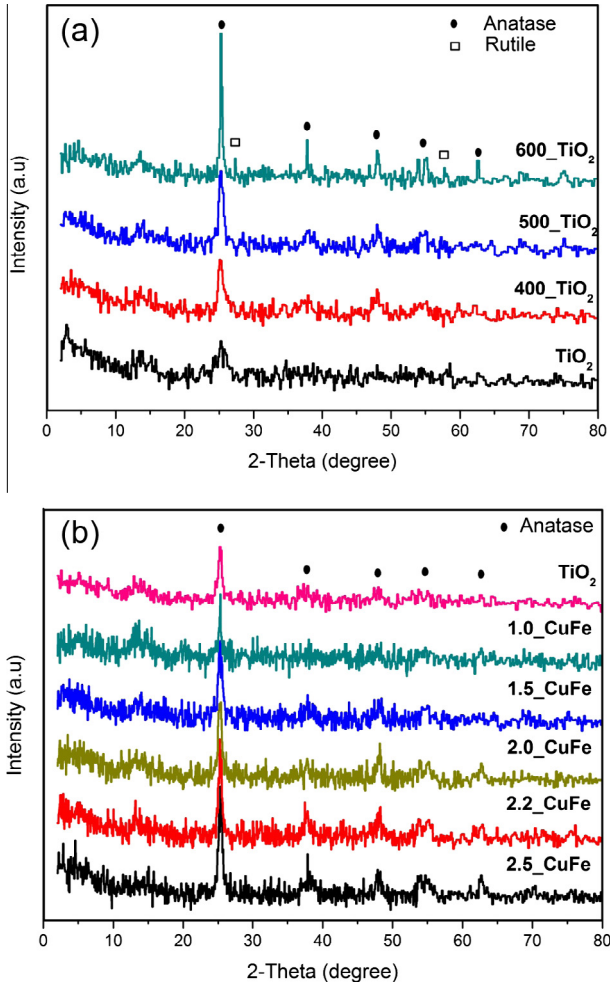


**Fig. 2.** XRD patterns of (a) raw $TiO_2$, 400_ $TiO_2$, 500_ $TiO_2$, and 600_ $TiO_2$ and (b) Cu–Fe/$TiO_2$ photocatalysts with different total metal loading (Cu:Fe mass composition = 10:1).

### 2.3. Preparation of Cu–Fe/$TiO_2$

A series of Cu–Fe/$TiO_2$ photocatalysts with different total metal loading (1.0, 1.5, 2.0, 2.2 and 2.5 wt%) was prepared using aqueous wet impregnation method. Based on the XRD patterns of the calcined $TiO_2$; 400_$TiO_2$, 500_$TiO_2$ and 600_$TiO_2$ reported in Section 3.1.2 and Fig. 2(a), 500_$TiO_2$ was used as the support. The photocatalysts were prepared with Cu:Fe mass composition fixed at 10:1. $CuCl_2{\cdot}2H_2O$ and $FeCl_3$ were used as metal precursors. Predetermined amounts of $CuCl_2{\cdot}2H_2O$ and $FeCl_3$ salts were dissolved in distilled water with continuous stirring. Then, the required amount of 500_$TiO_2$ support was added into the metal salt solution. The suspension was stirred for 1 h before the solvent was evaporated in a water bath at 80 °C and further dried in an oven at 120 °C for 18 h. The raw photocatalysts were ground into fine powder and then calcined at 500 °C for 1 h (10 °C $min^{-1}$ ramping). The temperature selected was adopted from previous reported method [26]. The denotation of the photocatalysts was: a_CuFe, where 'a' represents the total Cu–Fe metal loading in wt%, for example, 2.0_CuFe represents 2.0 wt% of total metal loading.

### 2.4. Characterization of photocatalysts

Thermogravimetric analysis on the raw and calcined $TiO_2$ was conducted using thermal gravimetry analyzer (TGA, Perkin Elmer, Pyris 1). The X-ray diffraction (XRD) patterns of the raw and calcined $TiO_2$ and also the prepared Cu–Fe/$TiO_2$ photocatalysts were recorded using Bruker D8 Advance with Cu Kα radiation (40 kV, 40 mA) at $2\theta$ angles from 2° to 80° and a scan speed of 4 °C $min^{-1}$ to determine the active $TiO_2$ phase present. Morphology of the photocatalysts were examined using field emission scanning electron microscopy (FESEM, Supra55VP) coupled with energy dispersive X-ray analysis (EDX) and high resolution transmission electron microscopy (HRTEM, Zeiss Libra 200). The light absorption properties of the photocatalysts were recorded using diffuse reflectance UV–visible spectroscopy (DR-UV–Vis) where the Shimadzu Spectrometer 3150 was equipped with an integrated sphere assembly in which $BaSO_4$ was used as the reference material. Tauc Plot, derived from DR-UV–Vis spectrum was employed to determine the band gap energy of the photocatalysts.

### 2.5. Photooxidative–extractive deep desulfurization process

The photooxidative–extractive deep desulfurization process for the removal of sulfur species involved suspending the photocatalyst in model oil containing dibenzothiophene (DBT) as the model sulfur species in dodecane. Photooxidation was carried out in a glass photo-reactor positioned below the light source (500 W halogen lamp, $\lambda > 400$ nm) at a distance of 15 cm between the lamp and the top of the photo-reactor. Two phases of reactions were conducted where in the first phase, adsorption–desorption equilibrium between the model oil and the photocatalyst took place in the dark. Subsequently, photooxidation process occurred under visible light illumination in the presence of $H_2O_2$. The model oil was mixed with 1 g $L^{-1}$ of photocatalyst. Then $H_2O_2$ with a molar ratio of 4:1 ($H_2O_2$:S) was added and the suspension was stirred in the dark for 30 min before the light was switched on. Periodic sampling was conducted where the photocatalyst was separated from the model oil by filtration prior to analysis using GC-SCD (Agilent 7890A gas chromatograph coupled with Agilent 355 sulfur chemiluminescence detector). It was equipped with DB-1 J & W 123–1033 column (30 m × 320 μm × 1 μm) maintained at 325 °C with helium as carrier gas flow rate of 1.1 mL $min^{-1}$. The auto sampler was in split mode (300 °C, 6.1629 psi, 50:1 split ratio at 55 mL $min^{-1}$, split flow 50 mL $min^{-1}$, septum purge flow 3 mL $min^{-1}$) and injection volume of 1.0 μL. The detector settings were: burner at 800 °C (to ensure complete sulfur combustion), dual plasma controller at 250–400 torr, 65 sccm of air flow rate, 40 sccm of $H_2$ flow rate and 20–30 mL $min^{-1}$ at 3–6 psi of ozone flow rate. The oxidized DBT, which is DBT sulfone ($DBTO_2$) was removed in the second phase by extraction using the CG IL. Parameters such as the total Cu–Fe metal loading, $H_2O_2$ amount, photocatalyst loading and initial DBT concentration were investigated.

The best performing photocatalyst was also employed for photooxidative–extractive deep desulfurization process on actual diesel fuel (309 ppm of sulfur species). The efficiency in converting sulfur species to oxidized sulfur species in both model oil and actual diesel was calculated using Eq. (1):

$$\text{Sulfur conversion } (\%) = \frac{S_i - S_f}{S_i} \times 100\% \quad (1)$$

where $S_i$ and $S_f$ refer to the initial and final concentrations of sulfur species in model oil (DBT) or actual diesel fuel, respectively, determined using GC-SCD. For extraction, CG IL was added to the model oil (or actual diesel fuel) filtrate in a volume ratio of 1:5 (CG IL:model oil filtrate or diesel fuel filtrate). The upper layer, being the filtrate was analyzed using GC-SCD to determine the percentage of sulfur species and oxidized sulfur species extracted. Both sulfur species and oxidized sulfur species were extracted using CG IL,

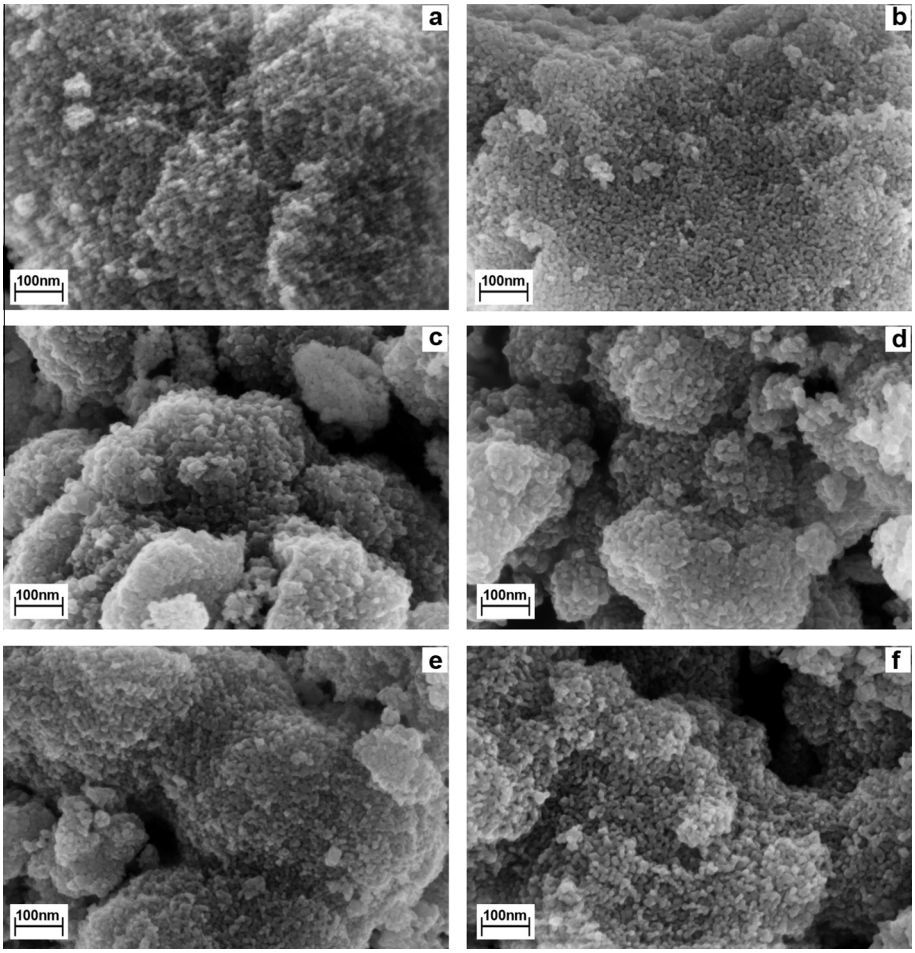


**Fig. 3.** FESEM micrographs of (a) 500_$TiO_2$, (b) 1.0_CuFe, (c) 1.5_CuFe, (d) 2.0_CuFe, (e) 2.2_CuFe and (f) 2.5_CuFe at 100 kX magnification.

although the CG IL had higher selectivity for oxidized sulfur species which is more polar. The extraction efficiency is given in Eq. (2):

$$\text{Extraction efficiency } (\%) = \frac{S_{BE} - S_{AE}}{S_{BE}} \times 100\% \quad (2)$$

where $S_{BE}$ and $S_{AE}$ refer to the total concentration of sulfur species and oxidized sulfur species in the model oil or actual diesel fuel before and after extraction with CG IL, respectively. For the system's efficiency in total sulfur removal, Eq. (3) was used:

$$\text{Sulfur removal } (\%) = \frac{S_i - S_{AE}}{S_i} \times 100\% \quad (3)$$

where $S_i$ and $S_{AE}$ refers to the initial concentration of sulfur species and final total concentration of sulfur species and oxidized sulfur species in the model oil (DBT and $DBTO_2$) or actual diesel fuel after extraction with CG IL.

## 3. Results and discussion

### 3.1. Characterization of $TiO_2$ and Cu–Fe/$TiO_2$

#### 3.1.1. TGA

The thermogram of raw $TiO_2$ is shown in Fig. 1(a). The first weight loss (11%) occurred between 50 °C and 155 °C depicting the removal of physically adsorbed water [27]. A second weight loss occurred between 155 °C and 240 °C, corresponding to a total weight loss of 10%. This may be attributed to the decomposition of residual organics. The third weight lose (5%) was slower compared to the two previous decomposition occurring from 240 to 550 °C. The total weight loss observed was 26%. A steady horizontal line indicates no further weight loss. TGA profile was used to estimate the calcination temperature range (400–600 °C) for the activation of the raw $TiO_2$ [28]. The thermogram for $TiO_2$ calcined at 500 °C for 1 h can be seen in Fig. 1(b). It can be observed that only 5% of weight loss was detected between 50 and 400 °C which was attributed to the physical absorbed moisture present in the sample. Therefore, heat treatment of the raw $TiO_2$ at 500 °C for 1 h was enough to completely remove any residues entity in the sample.

#### 3.1.2. XRD

XRD patterns of raw and calcined $TiO_2$ were shown in Fig. 2(a). Raw $TiO_2$ displayed very weak anatase phase. As the calcination temperature increased, the intensity of the anatase peaks increased. All the samples displayed typical anatase $TiO_2$ crystal structure with $2\theta$ peaks at 25.3°, 38.0°, 48.3°, 54.8°, 55.8° and 62.6° corresponding to (101), (004), (200), (105), (211) and (204) planes, respectively [29]. When the photocatalyst was calcined at 600 °C, rutile phase ($2\theta = 27.3°$) appeared which signifies a complete crystallization of the anatase phase. Phase transformation of anatase to rutile generally is unfavourable because it reduces the photocatalytic activity [30]. Based on these results, 500 °C was selected as the optimum calcination temperature for further studies [31].

The effect of Cu–Fe metal loading on the crystallite phase and crystallinities of the photocatalyst were also analyzed. Fig. 2(b) displays the XRD patterns of Cu–Fe/$TiO_2$ with different total metal loading of the Cu–Fe (1.0, 1.5, 2.0, 2.2 and 2.5 wt% at 10:1 mass composition of Cu:Fe). All the samples displayed typical anatase

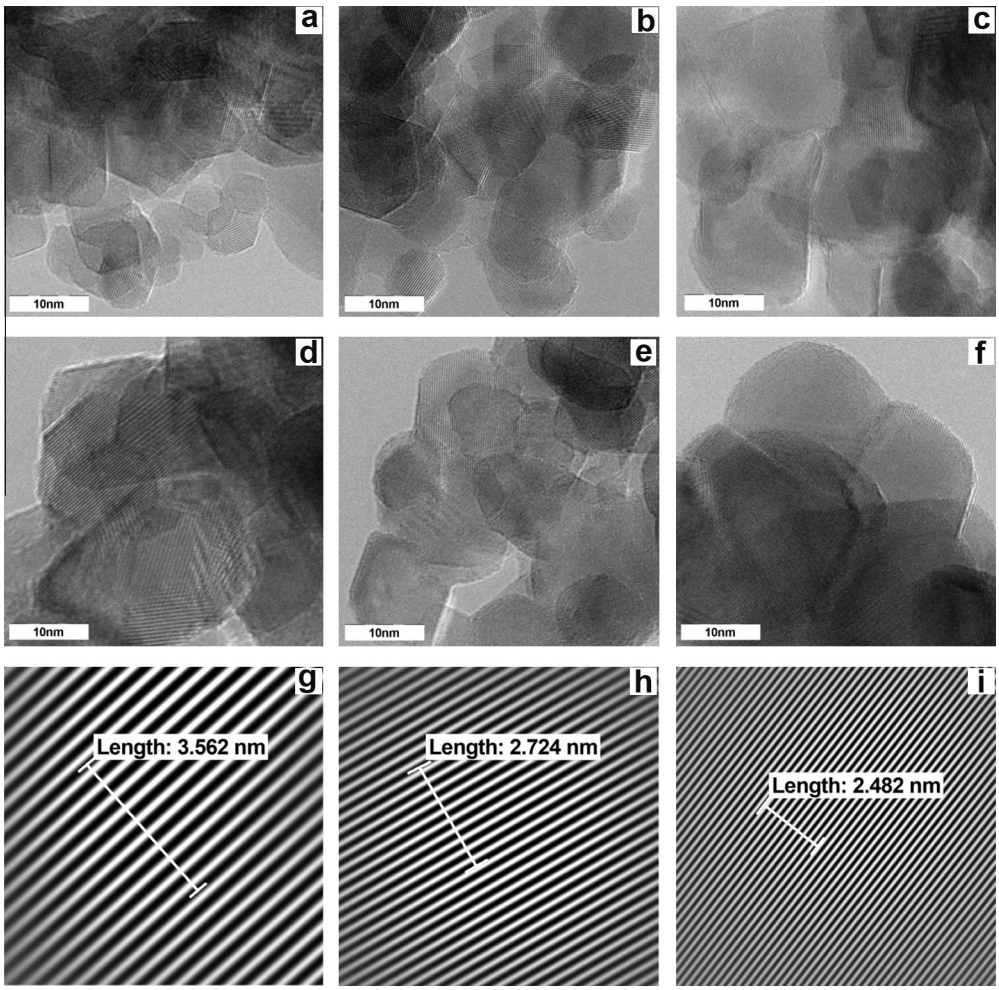


**Fig. 4.** HRTEM micrographs of (a) 500_$TiO_2$, (b) 1.0_CuFe, (c) 1.5_CuFe, (d) 2.0_CuFe, (e) 2.2_CuFe, (f) 2.5_CuFe; and lattice fringes of 2.0_CuFe for (g) anatase $TiO_2$ (1 0 1), (h) CuO (1 1 0) and (i) $Fe_2O_3$ (3 1 1).

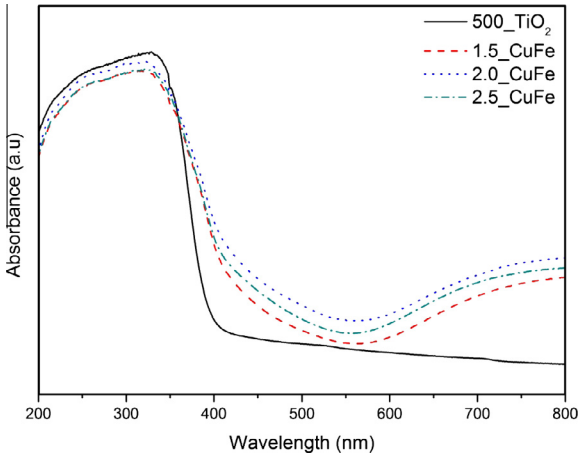


**Fig. 5.** DR-UV–Vis spectra of 500_$TiO_2$ and Cu–Fe/$TiO_2$ photocatalysts with different total metal loading (Cu:Fe mass composition = 10:1).

$TiO_2$ crystal structure. The dominant peak at $2\theta = 25.3°$ representing $TiO_2$ anatase (1 0 1) plane was observed in all the samples. In Fig. 2(b), it could be seen that increasing the total metal loading increased the dominant peak intensity. No indications of the presence of Cu, Fe or Cu–Fe species in all the XRD patterns. This may be due to high dispersion of Cu and Fe species and also the low metal content [32], which are below the detection limit of the equipment [33]. In order for the metal to be detectable by XRD analysis, the concentration of metals should be higher than 5 wt% [34]. It can also be seen that there are no peaks attributed to the rutile phase. This might be due to the calcination temperature, as the transition from anatase to the rutile phase normally occurs at temperature above 600 °C.

The dominant anatase peak ($2\theta = 25.3°$) was used to estimate the crystallite size of the photocatalysts using Debye Scherrer's equation shown in Eq. (4) [35].

$$D = \frac{K\lambda}{\mathrm{FWHM}\cos\theta} \tag{4}$$

where $D$ is the crystallite size, $K$ is the Scherrer constant which accounts for the shape of the particles and is generally taken to have the value of 0.89 [29], $\lambda$ is the wavelength of the X-ray, FHWN is the full width at half maximum of the reflection peak that has the same maximum intensity in the diffraction pattern, and $\cos\theta$ is the diffraction angle. The estimated crystallite size for raw $TiO_2$ was 5.75 nm. The crystallite size increased from 10.42 to 11.50 and 26.84 nm for $TiO_2$ calcined at 400, 500 and 600 °C, respectively. All photocatalysts doped with metal displayed high intensity for the diffraction peak at $2\theta = 25.3°$ (1 0 1), signalling larger crystal size compared to $TiO_2$ photocatalyst without metal doping. As the total metal loading increased from 1.0 wt% to 2.5 wt%, an increasing trend in the crystallite size was observed. 2.5_CuFe showed the

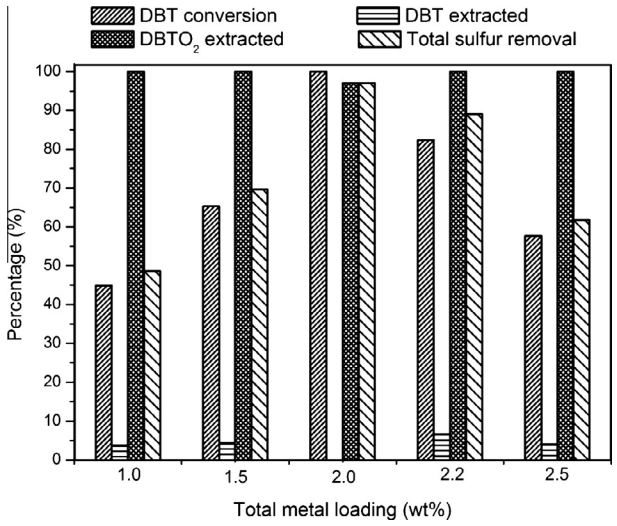


**Fig. 6.** Effect of total Cu–Fe metal loading on deep desulfurization performance (Cu:Fe mass composition = 10:1).

largest crystallite size of 20.13 nm. The average crystallite size for 1.0_CuFe, 1.5_CuFe, 2.0_CuFe and 2.2_CuFe were 13.42, 14.07, 16.11 and 17.42 nm, respectively. The increase in crystallite size may be ascribed to the increase in total metal loading and to the increased agglomeration between Cu, Fe and $TiO_2$ particles during calcination [36].

### 3.1.3. FESEM and HRTEM

The morphologies of the photocatalysts such as crystallite shape, size, and metal dispersion were determined by FESEM-EDX and HRTEM. Fig. 3(a–f) displays the FESEM micrographs of bare $TiO_2$ and Cu–Fe/$TiO_2$ at different metal loadings. The particles of bare $TiO_2$ were small compared to the metal doped photocatalysts with average particle size of 11.39 nm. As the total metal loading of Cu–Fe increased from 1.0, 1.5, 2.0, 2.2 and 2.5 wt%, the average particle size also increased from 13.09, 14.51, 15.59, 17.33 and 20.53 nm, respectively. The morphology of the particles was spherical with increased agglomeration when the total metal loading of Cu and Fe increased [37]. No localized metal particles were detected, indicating high metallic dispersion of Cu and Fe on the $TiO_2$. This observation is in agreement with the results from XRD.

EDX is used to qualitatively and quantitatively analyze the elements present in a selected area of the FESEM image. Mapping of 2.0_CuFe shows very clearly that the Cu and Fe metal dopant were well dispersed showing uniform distribution onto the surface of $TiO_2$. As mentioned before, the presence of Cu and Fe metals were not detected by XRD because of the well dispersed small crystallite size of the metal species on the photocatalyst, enhancing the photocatalytic activity [38]. Similar mapping images were obtained for other photocatalysts, showing that the preparation method has successfully incorporated Cu and Fe onto the $TiO_2$ surface.

Image processing analysis of HRTEM micrographs were used to achieve the refinement of microstructure for more accurate analysis of single grains and grains boundaries. Fig. 4(a–f) displays the HRTEM micrographs of Cu–Fe/$TiO_2$ photocatalysts at different total metal loading. The estimated particle size were 10.11–15.91, 11.32–15.02, 11.78–16.93, 13.51–20.67 and 15.38–22.19 nm for 1.0, 1.5, 2.0, 2.2 and 2.5 wt%, respectively These particle sizes are in good agreement with the average particle size obtained from FESEM data. HRTEM micrographs of the photocatalysts suggest that particles in the photocatalysts tend to stick to each other. This is possible due to high content of surface hydroxyl groups contributing toward the hydrophilic properties [39]. The lattice fringes of 2.0_CuFe photocatalyst are displayed in Fig. 4(g–i) with d-spacing of 0.36 nm that can be attributed to the (1 0 1) plane of the anatase $TiO_2$ phase [40]. There is no sight of lattice fringe related to rutile $TiO_2$. This is in agreement to the results from XRD which showed only anatase phase. In addition to that, the lattice fringes of 0.27 nm and 0.25 were observed which could be ascribed to the (1 1 0) plane of CuO [41] and (3 1 1) plane of $Fe_2O_3$ [42].

### 3.1.4. DR-UV–Vis

Fig. 5 shows the DR-UV–Vis absorption spectra of photocatalysts with different total metal loading, together with 500_$TiO_2$. The absorption spectrum for 500_$TiO_2$ showed an absorption edge at 400 nm corresponding to the band gap of 3.09 eV. When $TiO_2$ was doped with 1.0 wt% Cu–Fe, a large shift of the absorbance edge was observed which is in agreement with the color change of the photocatalyst from white powder to yellowish green due to the presence of Fe and Cu. This significant shift of the edge could also be seen for 1.5_CuFe, 2.2_CuFe and 2.5_CuFe. 2.0_CuFe displayed the largest shift. All the spectra indicated that the Cu–Fe/$TiO_2$ photocatalysts display better visible light absorption compared to synthesized $TiO_2$. All of the doped $TiO_2$ shows extended absorption spectra into visible region in the range from 400 to 800 nm. Cu–Fe doped $TiO_2$ sample showed substantial and broader absorption shoulder up to 800 nm. The extended absorption of Cu–Fe/$TiO_2$ samples into the visible region has been explained in terms of excitation of electrons of dopant ion to $TiO_2$ conduction band. For example, the enhanced absorption observed for the metal doped

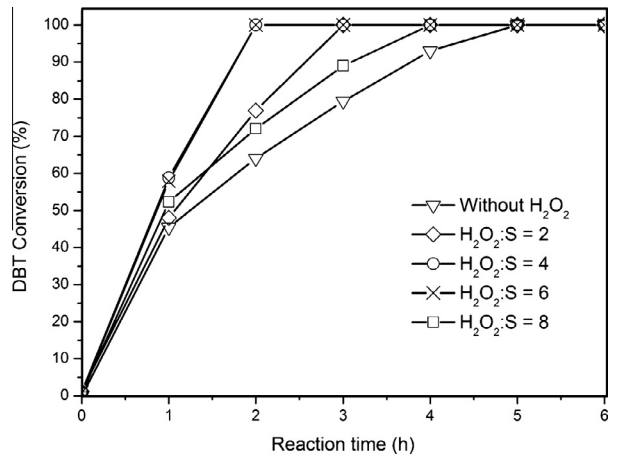


**Fig. 7.** Effect of different $H_2O_2$:S molar ratio on DBT conversion.

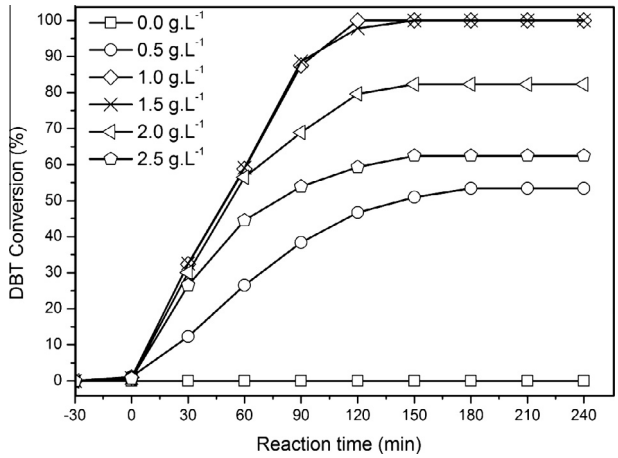


**Fig. 8.** Effect of photocatalyst loading on DBT conversion.

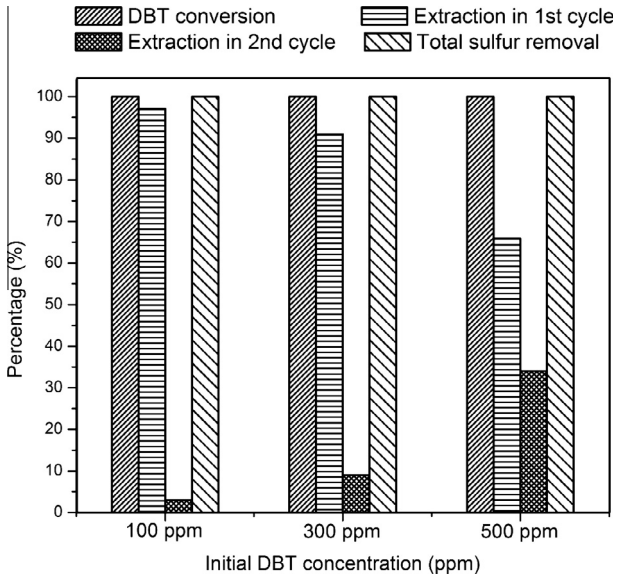


**Fig. 9.** DBT conversion and sulfur removal for different initial DBT concentration in model oil.

$TiO_2$ samples doped with Cu–Fe in the visible region can be considered to involve excitation of 3d electrons of dopant ion to $TiO_2$ conduction band according to their respective energy levels [43,44]. The enhancement of light absorption in the visible region provides a possibility for improving the photocatalytic performance of $TiO_2$ under visible light irradiation. Doping with Cu–Fe could create subband states in the band gap of $TiO_2$ which can then be easily excited to produce more electron–hole pairs under visible light irridation, hence resulting in higher photocatalytic performance compared to un-doped $TiO_2$ [44].

In order to determine the band gap energy of the photocatalysts, reflectance [F(R)] spectra using Kubelka–Munk formalism and Tauc plot was employed for each synthesized photocatalysts [45]. Using the Tauc plot of $[F(R).h\nu]^n$ vs. $h\nu$ where $h\nu$ is the photon energy and $n = ½$ for direct band gap of the photocatalyst, the linear region of the plot was extrapolated to intersect on the photon energy axis to deduce the band gap energy of the photocatalyst. The band gap of bare $TiO_2$ was 3.09 eV but upon incorporation of Cu and Fe (2.0_CuFe), the value was reduced to 2.69 eV. The band gap for 1.0_CuFe, 1.5_CuFe, 2.2_CuFe and 2.5_CuFe were 2.75, 2.77, 2.70 and 2.75 eV, respectively. The blue shift in the absorption of photocatalysts suggested that the dopants successfully generate lower energy level between the valence and conduction bands [34]. The estimated band gap energy of metal doped $TiO_2$ was lower compared to $TiO_2$ P25 (3.2 eV) [46]. Decrease in the band gap energy increases the absorbance in the visible region and indicates that the electron–hole pairs can be generated with metal doping on the $TiO_2$, which can be attributed to the charge transfer transition between metal ions and $TiO_2$ in the conduction or valence band [47].

### 3.2. Photooxidative–extractive deep desulfurization performance

#### 3.2.1. Effect of total metal loading

The photocatalytic activity was investigated using 100 ppm model oil. The total percentage of sulfur conversion was determined as the photocatalyst performance indicator. The findings are depicted in Fig. 6. It could be seen that the lowest performance of the system was obtained using 1.0_CuFe (44.87% DBT conversion, 3.77% DBT extracted, 100% $DBTO_2$ extracted and 48.64% total sulfur removal). Increasing the total metal loading to 1.5 wt% and 2.0 wt% enhanced DBT conversion to 65.33% and 100%, respectively, with total sulfur removal of 69.67% and 97.06%, respectively. At higher total metal loading (>2.0 wt%), the particles were highly agglomerated, thus reducing the surface area available for photooxidation process. From these results, the best total metal loading was identified as 2.0 wt% and 2.0_CuFe was used for further studies.

#### 3.2.2. Effect of $H_2O_2$ amount

The addition of an oxidant has proven to enhance the photooxidation efficiency. Fig. 7 shows the DBT conversion for different $H_2O_2$:S molar ratios. Without the addition of $H_2O_2$, it took 5 h for the DBT conversion to reach 100%. When the amount of $H_2O_2$:S used was 2 and 4, the time taken for DBT conversion reduced. Both reached 100% DBT conversion within 3 h and 2 h, respectively. Two DBT conversion curves almost coincided with little change in the values, when the $H_2O_2$:S molar ratio was 4 and 6. Again both showed 100% DBT conversion in 2 h. This showed that the dosage of $H_2O_2$ was excessive when $H_2O_2$:S molar ratio was 6. Increasing further the $H_2O_2$:S molar ratio to 8, the time taken to reach 100% was increased to 4 h. This might be caused by the formation of excessive amount of gas upon irradiation of large amount of $H_2O_2$ that could hamper the adsorption of reactant on the photocatalyst surface to reduce the reaction probability, which functions as a scavenger of ·OH free radicals, leading to an increase in the reaction time [48]. The $H_2O_2$:S molar ratio of 4 was selected for further studies because of the shortest time taken for complete DBT conversion.

#### 3.2.3. Effect of photocatalyst loading

The optimum photocatalyst loading must be determined in order to avoid excess catalyst and to ensure total absorption of photons. Optimum loading corresponds to the maximum amount of photocatalyst needed to achieving total surface illumination. The effect of photocatalyst loading was investigated by keeping constant other parameters such as: $H_2O_2$:S molar ratio of 4 and initial DBT concentration of 100 ppm. The range of photocatalyst loading tested was between 0.5–2.5 g $L^{-1}$, as seen in Fig. 8. The lowest DBT conversion was at photocatalyst loading of 0.5 g $L^{-1}$ with 53.4% DBT conversion. DBT conversion reached 100% for photocatalyst loading of 1.0 and 1.5 g $L^{-1}$. The higher DBT conversion may be due to the increased availability of surface area. This increases the adsorption sites, which directly increases the adsorption of photon and also increases the concentration of active species. Increasing the photocatalyst loading to 2.0 and 2.5 g $L^{-1}$ decreased the DBT conversion to 82.3 and 62.5%, respectively, indicating that overdosing the photocatalyst has negative influence on DBT conversion. This may be due to low penetration of light into the solution and high light scattering caused by the high concentration of photocatalyst, which can decrease the DBT conversion and thus reduce the overall performance. In addition, the photocatalyst tends to agglomerate and settle down at higher concentration. From the results, the optimum photocatalyst loading was be determined as 1 g $L^{-1}$.

#### 3.2.4. Effect of initial DBT concentration

Under the same conditions, DBT conversions for different initial DBT concentrations are shown in Fig. 9. It was clear that that the DBT conversion in all the model oils with 100, 300 and 500 ppm of DBT was 100%. Fig. 9 also shows the amount of $DBTO_2$ extracted in the first run, second run and also the total sulfur (DBT and $DBTO_2$) removal. For initial concentration of 100 ppm DBT, 97.06% of the $DBTO_2$ was extracted in the first run and 2.94% in the second. The total removal was 100% after two cycles of extraction. The same trend could be observed for concentrations of 300 and 500 ppm DBT, where in the first run 91.02% and 65.91% of $DBTO_2$ was extracted followed by 8.98% and 34.09% in the second

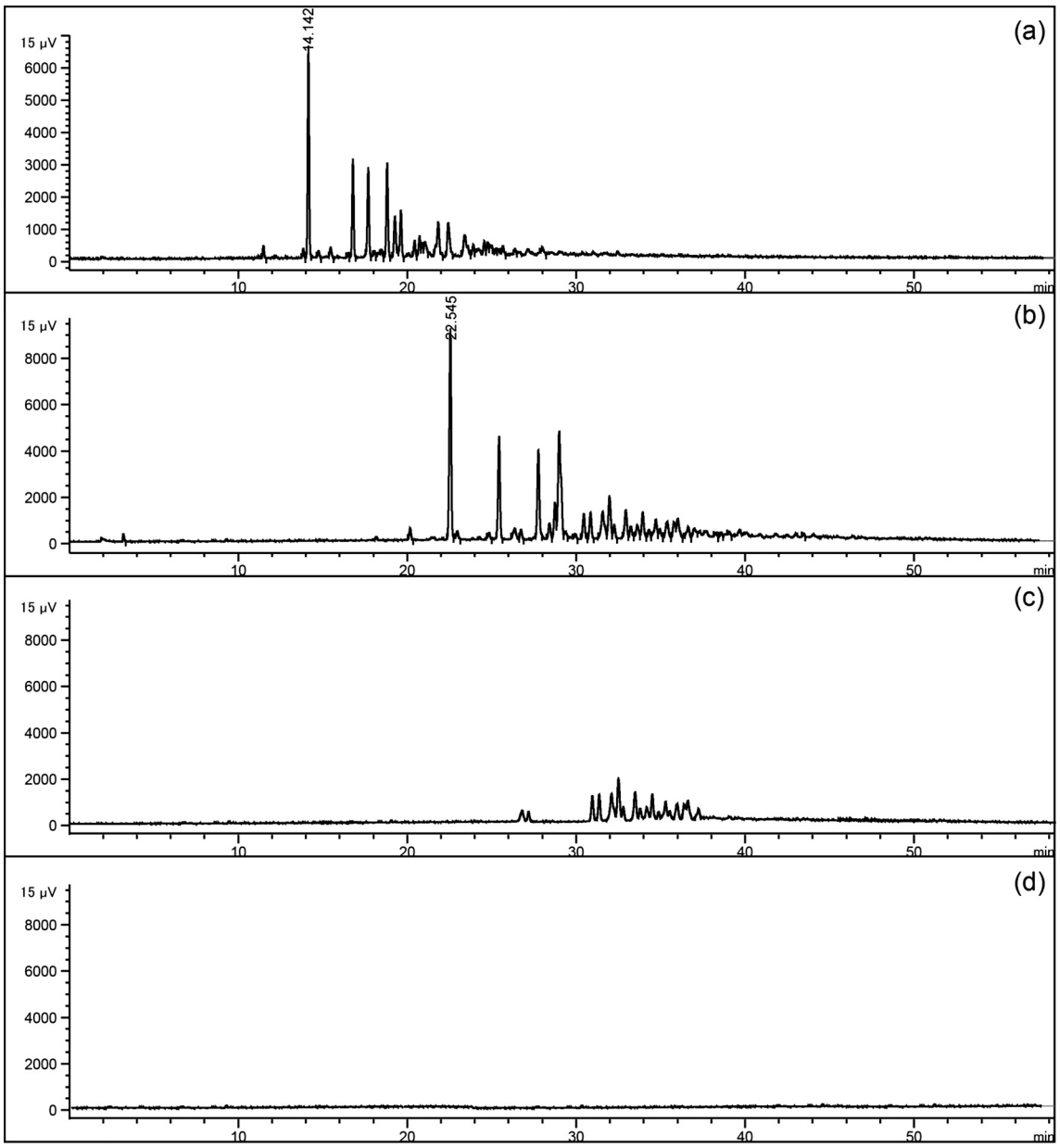


**Fig. 10.** GC analysis of sulfur species in diesel fuel (a) before oxidation and (b) after oxidation using 2.0_CuFe/$TiO_2$ and after extraction for the (c) first extraction and (d) second extraction with CG IL.

run for 300 and 500 ppm DBT, respectively. It can also be seen that when increasing the DBT concentration, the extraction of the oxidized sulfur species becomes less efficient.

*3.2.5. Recycling of 2.0_CuFe photocatalyst*

After the reaction, the photocatalyst was washed with water, filtered and then dried in the oven at 120 °C. Under similar reaction conditions, six recycling runs using the washed photocatalyst showed 99.5–100% sulfur conversion with an average recyclability of 99.75%.

*3.2.6. Sulfur removal from actual diesel fuel*

Under the same conditions as the model oil, photooxidative–extractive deep desulfurization was carried out on actual diesel fuel. After 3 h, the sulfur conversion in actual diesel fuel reached 100%. In the first extraction 78.93% of oxidized sulfur species was extracted followed by 21.07% in the second extraction. The extraction was conducted in two cycles as the first extraction could only remove 78.93% of the oxidized sulfur species. This may be due to the saturation of oxidized sulfur species in the CG IL, preventing further extraction of the oxidized sulfur species. In the second cycle, the remaining oxidized sulfur species could be removed giving a total sulfur removal of 100%. Fig. 10(a) and (b) show the GC chromatograms of actual diesel fuel before and after photooxidation, respectively. As can be seen in the figures, all the sulfur species peaks from actual diesel fuel were shifted indicating that the sulfur species have been fully oxidized. Fig. 10(c) and (d) displays the GC chromatograms of actual diesel fuel after the first and second extraction with CG IL, respectively. It can be seen that the peaks intensity in Fig. 10(c) has reduced and in Fig. 10(d) there was no sulfur peaks detected indicating complete sulfur removal.

## 4. Conclusion

In summary, Cu–Fe/$TiO_2$ photocatalysts were synthesized using wet-impregnation method. It was shown that the photocatalytic

activity of Cu–Fe/$TiO_2$ was better than that of bare $TiO_2$ photocatalyst. Sulfur conversion using 2.0_CuFe could reach 100% conversion within 2 h. The optimum experimental conditions proposed were: $H_2O_2$:S = 4, and 1 $g{\cdot}L^{-1}$ photocatalyst loading. The photocatalyst could be recycled and reused with an average recyclability of 99.75%. 2.0_CuFe could also reach 100% sulfur conversion when used on actual diesel fuel. The photooxidative–extractive method using 2.0_CuFe and CG IL gave 100% sulfur removal.

## Acknowledgements

The authors would like to express their gratitude for the financial and facilities support provided by Yayasan UTP, MyPhD and FRGS from the Ministry of Education, Malaysia; and the Centre of Research in Ionic Liquid (CORIL), Universiti Teknologi PETRONAS.

## References

[1] Villasen F, Loera O, Campero A, Viniegra-Gonzalez G. Oxidation of dibenzothiophene by laccase or hydrogen peroxide and deep desulfurization of diesel fuel by the later. Fuel Process Technol 2004;86:49–59.
[2] Zhang J, Zhao DS, Wang JL. Photocatalytic oxidation of dibenzothiophene using $TiO_2$/bamboo charcoal. J Mater Sci 2009;44:3112–7.
[3] Stanislaus A, Marafi A, Rana MS. Recent advances in the science and technology of ULSD production. Catal Today 2010;153:1–68.
[4] Lina Y, Jian L, Xingdong Y, Shen J, Yutai Q. One step non-hydrodesulfurization of fuel oil: catalyzed oxidation adsorption desulfurization over HPWA-SBA-15. J Mol Catal A: Chem 2007;262:114–8.
[5] Lu H, Deng C, Ren W, Yang X. Oxidative desulfurization of model diesel using $[(C_4H_9)_4N]_6Mo_7O_{24}$ as a catalyst in ionic liquids. Fuel Process Technol 2014;119:87–91.
[6] Ban LL, Liu P, Ma CH, Dai B. Deep extractive desulfurization of diesel fuel by $FeCl_3$/ionic liquids. Chinese Chem Lett 2013;24:755–8.
[7] Rodriguez-Cabo B, Rodriguez H, Rodil E, Arce A, Soto A. Extractive and oxidative–extractive desulfurization of fuel with ionic liquids. Fuel 2014;117:882–9.
[8] Dinamarca MA, Ibacache-Quiroga C, Baeza P, Galvez S, Villarroel M, Olivero P, et al. Biodesulfurization of gas oil using inorganic supports biomodified with metabolically active cells immobilized by adsorption. Bioresource Technol 2010;101:2375–8.
[9] Fatemeh DD, Manouchehr V, Abed AZ. Biodesulfurization of dibenzothiophene by newly isolated rhodococcus erythropolis strain. Bioresource Technol 2010;101:1102–5.
[10] Li WL, Tang H, Liu Q, Xing J, Li Q, Wang D, et al. Deep desulfurization of diesel by integrating adsorption and microbial method. Biochem Eng J 2009;44:297–301.
[11] Kim H, Ma X, Zhou A, Song C. Ultra-deep desulfurization and denitrogenation of diesel fuel by selective adsorption over three different adsorbents: a study on adsorptive selectivity and mechanism. Catal Today 2006;111:74–83.
[12] Lu H, Ren W, Wang H, Wang Y, Chen W, Suo Z. Deep desulfurization of diesel by ionic liquid extraction coupled with catalytic oxidation using Anderson-type catalyst $[(C_4H_9)_4N]_4NiMo_6O_{24}H_6$. Appl Catal A: Gen 2013;453:376–82.
[13] Lu H, Zhang Y, Jiang Z, Li C. Aerobic oxidative desulfurization of benzothiophene, dibenzothiophene and 4,6-dimethyldibenzothiophene using an Anderson-type catalyst $[(C_{18}H_{37})_2N(CH_3)_2]_5[IMo_6O_{24}]$. Green Chem 2010;12:1954–8.
[14] Matsuzawa S, Tanaka J, Sato S, Ibusuki T. Photocatalytic oxidation of dibenzothiophene in acetonitrile using $TiO_2$: effect of hydrogen peroxide and ultrasound irradiation. J Photochem Photobio A 2002;149:183–9.
[15] Zhao Y, Zhao L, Han J, Xu YY, Wang SQ. Study on method and mechanism for simultaneous desulfurization and denitrification of flue gas based on the $TiO_2$ photocatalysis. Sci China Ser E-Tech Sci 2008;51:268–76.
[16] Na P, Zhao B, Gu L, Liu J, Na J. Deep desulfurization of model gasoline over photoirradiated titanium-pillared montmorillonite. J Phys Chem Solids 2009;70:1465–70.
[17] Zhang D. Enhanced photocatalytic activity for titanium dioxide by co-modification with copper and iron. Transit Metal Chem 2010;35:933–8.
[18] Liu J, Zhang Z, Yang L, Zhang Y, Deng S. The degradation of reactive black wastewater by Fe/Cu co-doped $TiO_2$. Int J Chem 2011;3:87–92.
[19] Kędra-Krolik K, Mutelet F, Moise JC, Jaubert JN. Deep fuels desulfurization and denitrogenation using 1-butyl-3-methylimidazolium trifluoromethanesulfonate. Energy Fuels 2011;25:1559–65.
[20] Kędra-Krolik K, Mutelet F, Moise JC, Jaubert JN. Extraction of thiophene or pyridine from n-heptane using ionic liquids. Gasoline and diesel desulfurization. Ind Eng Chem Res 2011;50:2296–306.
[21] Zhao Y, Hao YJ, Li FT. Photocatalytic oxidation desulfurization of fuel using nano-$TiO_2$ in ionic liquid. Adv Mater Res 2011;282–283:599–602.
[22] Abbott AP, Cullis PM, Gibson MJ, Harris RC, Raven E. Extraction of glycerol from biodiesel into a eutectic based ionic liquid. Green Chem 2007;9:868–72.
[23] Jhong HR, Wong SDH, Wan CC, Wang YY, Wei TC. A novel deep eutectic solvent-based ionic liquid used as electrolyte for dye-sensitized solar cells. Electrochem Comm 2009;11:209–11.
[24] Ma X, Velu S, Kim JH, Song C. Deep desulfurization of gasoline by selective adsorption over solid adsorbents and impact of analytical methods on ppm-level sulfur quantification for fuel cell application. Appl Catal B: Environ 2005;56:137–47.
[25] Khan MA, Akhtar MS, Yang OB. Synthesis, characterization and application of sol–gel derived mesoporous $TiO_2$ nanoparticles for dye-sensitized solar cells. Sol Energy 2010;84:2195–201.
[26] Zaid HFM, Chong FK, Mutalib MIA. Integrated photooxidative–extractive desulfurization system for fuel oil using Cu, Fe and Cu–Fe/$TiO_2$ and eutectic based ionic liquids: effect of calcination temperature and duration. AIP Conf Proc 2014;1621:231–7.
[27] Tanaka H, Sadamoto T. The simultaneous determination of the kinetics and thermodynamics of $Cu(OH)_2$ decomposition by means of TG and DSC. Thermochim Acta 1982;54:273–80.
[28] Moura JA, Araujo AS, Coutinho ACSLS, Joana MFBA, Silva AOS, Souza MJB. Thermal analysis applied to characterization of copper and nickel catalysts. J Therm Anal Calorim 2005;79:435–8.
[29] Vijayalakshmi R, Rajendran V. Synthesis and characterization of nano-$TiO_2$ via different methods. Arch Appl Sci Res 2012;4:1183–90.
[30] Orlikowski J, Tryba B, Ziebro J, Morawski AW, Przepiorski J. A new method for preparation of rutile phase titania photoactive under visible light. Catal Commun 2012;24:5–10.
[31] Watthanaarun J, Pararajarn V, Supaphol P. Titanium (IV) oxide nanofibers by combined sol–gel and electrospinning techniques: preliminary report on effects of preparation conditions and secondary metal dopant. Sci Technol Adv Mater 2005;6:240–5.
[32] Kim DS, Kwak SY. The hydrothermal synthesis of mesoporous $TiO_2$ with high crystallinity, thermal stability, large surface area, and enhanced photocatalytic activity. Appl Catal A: Gen 2007;323:110–8.
[33] Yu J, Zhao X, Zhao Q. Effect of surface structure on photocatalytic activity of $TiO_2$ thin films prepared by sol–gel method. Thin Solid Films 2000;379:7–14.
[34] Wu Y, Zhang J, Xiao L, Chen F. Preparation and characterization of $TiO_2$ photocatalysts by $Fe^{3+}$ doping together with Au deposition for the degradation of organic pollutants. Appl Catal B: Environ 2009;88:525–32.
[35] Yoong LS, Chong FK, Dutta BK. Development of copper-doped $TiO_2$ photocatalyst for hydrogen production under visible light. Energy 2009;34:1652–61.
[36] Choi HJ, Kang M. Hydrogen production from methanol/water decomposition in a liquid photosystem using the anatase structure of Cu loaded $TiO_2$. Int J Hydrogen Energy 2007;32:3841–8.
[37] Xu S, Ng J, Zhang X, Bai H, Sun DD. Fabrication and comparison of highly efficient Cu incorporated $TiO_2$ photocatalyst for hydrogen generation from water. Int J Hydrogen Energy 2010;35:5254–61.
[38] Nurlaela E, Chong FK, Dutta BK, Riaz N. Bimetallic Cu–Ni/$TiO_2$ as photocatalyst for hydrogen production from water. In: International conference on fundamental and applied sciences (ICFAS2010). Kuala Lumpur, Convention Center, KL; 2010.
[39] AEROXIDE and AEROPERL. Technical information (1243) for Aeroxide and Aeroperl titanium Dioxide as photocatalyst; 2005. Bulletin No. 1-1243-0:1-14.
[40] Parra R, Goes MS, Castro MS, Longo E, Bueno PR, Varela JA. Reaction pathway to the synthesis of anatase via the chemical modification of titanium isopropoxide with acetic acid. Chem Mater 2008;20:143–50.
[41] Kannaki K, Ramesh PS, Geetha D. Hydrothermal synthesis of CuO nanostructure and their characterizations. Int J Sci Eng Res 2012;3:1–4.
[42] Chen W, Pan X, Willinger MG, Su DS, Bao X. Facile autoreduction of iron oxide/carbon nanotube encapsulates. J Am Chem Soc 2006;128:3136–7.
[43] Nahar MS, Hasegawa K, Kagaya S. Photocatalytic degradation of phenol by visible light-responsive iron-doped $TiO_2$ and spontaneous sedimentation of the $TiO_2$ particles. Chemosphere 2006;65:1976–82.
[44] Zhu J, Chen F, Zhang J, Chen H, Anpo M. $Fe^{3+}$–$TiO_2$ photocatalysts prepared by combining sol–gel method with hydrothermal treatment and their characterization. J Photochem PhotoBio A: Chem 2006;180:196–204.
[45] Murphy AB. Band-gap determination from diffuse reflectance measurements of semiconductor films, and application to photoelectrochemical water-splitting. Sol Energy Mater Sol Cells 2007;91:1326–37.
[46] Yalçın Y, Kılıç M, Çınar Z. $Fe^{+3}$-doped $TiO_2$: a combined experimental and computational approach to the evaluation of visible light activity. Appl Catal B: Environ 2010;99:469–77.
[47] Arias M, Laurenti D, Belliere V, Geanlet C, Vrinat M, Yoshimura Y. Preparation of supported $H_3PW_{12}0_{40}{\cdot}6H_2O$ for thiophenic compounds alkylation in FCC gasoline. Appl Catal A: Gen 2008;348:142–7.
[48] Xiaoming G, Wenhong L, Feng F, Yufei W, Dong L, Jiwu W. Preparation of $Bi_2WO_6$ photocatalyst and its application in the photocatalytic oxidative desulfurization. China Petrol Process Petrochem Technol 2011;13:19–23.